FRONTIERS OF PHYSICS

RESEARCH ARTICLE
Volume 19 / Issue 3 / 32201 / 2024

Curved anisotropic polaritons

Tao Hou[1,*], Yixiao Ge[1,*], Shuwen Xue[1], Huanyang Chen[1,2,†]

1 Department of Physics and Institute of Electromagnetics and Acoustics, Xiamen University, Xiamen 361005, China
2 Jiujiang Research Institute of Xiamen University, Jiujiang 332000, China
*These authors contributed equally to this work.
Corresponding author. E-mail: †kenyon@xmu.edu.cn
Received August 2, 2023; accepted October 12, 2023

ABSTRACT

The curved surface has emerged as new research platform for understanding and manipulating novel electromagnetic behaviors in complex media. In this paper, we explore the anisotropic polaritons on the spherical surface based on Maxwell's fish-eye metric through stereographic projection. Additionally, this phenomenon can be extended to spindle surface by conformal mapping. Our calculations and simulations demonstrate the elliptic and hyperbolic polaritons, excited by an electric dipole on the sphere, will self-focus or focus on the poles on the sphere affected by anisotropic permittivity. Furthermore, we reveal the optical singularity nature of the curved hyperbolic polaritons from the perspective of transformation optics by obtaining the equivalent optical refractive index profiles and the particle potential energy. Based on natural anisotropic materials and metamaterials, the curved polaritons have potential applications in curved surface focusing and chaos regulation. This work not only bridges the transformation optics and anisotropic polaritons at curved surface, but also provides a new route to surface optical field manipulation.

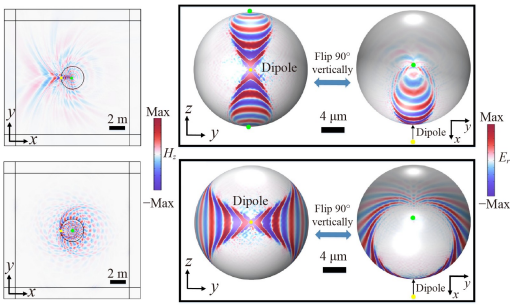

Keywords anisotropic polaritons, transformation optics, curved surface

1 Introduction

Polaritons [1, 2], are quasi-particles that arise from the interaction of photons and matter. They can break through the diffraction limit of light and compress light to the nanometer scale with small mode volume and strong photon state density, providing a unique way to manipulate light. In solids, electrons and excitons can be coupled with photons to form plasmon polaritons (PPs) and exciton polaritons. Surface plasmon polaritons (SPPs) are the most typical example, formed due to the interaction of free electrons and photons at the interface between metals and dielectric media [3–6]. While metal SPPs have been extensively studied and applied in various optical fields, the lifetime of the traditional metal SPPs become low due to the influence of the ohmic losses in plasmonic materials. Moreover, the operating frequency of mental SPPs is mainly limited to the near-infrared, visible and ultraviolet bands, leading to the lack of dynamic tuning capability. These factors greatly limit the application of metal SPPs. In addition, polaritons formed by optical phonons coupled with photons are called phonon polaritons (PhPs). In the last decade, two-dimensional van der Waals (vdW) layered materials have been developed as a promising polariton carriers, enabling the realization of polaritons in atomically thin materials. Two-dimensional materials have been shown to support the propagation of various highly localized polaritons with unique properties. For instance,

Higher Education Press

https://doi.org/10.1007/s11467-023-1360-9

adjustable SPPs can propagate in graphene and black phosphorus [7, 8], low-loss anisotropic PhPs can propagate in hexagonal boron nitride (hBN) and α-phase molybdenum trioxide (α-MoO_3) [9–11], while exciton polariton propagation can be observed in transition metal sulfur compounds (WSe_2, MoS_2) [12], and so on. Recently, anisotropic polaritons based on vdW heterostructures provide unprecedented control over the polaritonic responses, thereby enabling new nanophotonic applications [1, 13–15]. In addition, some layers or cylindrical lamellar metamaterials can be constructed to support the propagation of hyperbolic anisotropic polaritons [16, 17]. However, the manipulation of anisotropic polaritons in two-dimensional materials was mainly focused on planar systems, without considering the effect of curvature.

Controlling the light field on three-dimensional (3D) curved structures provides a higher degree of freedom and wider range of control compared to planar systems. Designing special three-dimensional structures or breaking the symmetry of existing ones has been successful in generating new phenomena or improving the performance of devices, such as optical wormholes [18] and chaotic microcavities with ultra-high Q values [19]. Furthermore, considering common 3D curved structures with special excitation methods and optical media are also effective approaches. For instance, the cylinder composed of hyperbolic metamaterial exhibits an abnormal focusing effect and can be used in optical focusing devices [20]. By adding orbital angular momentum to the cylindrical surface, it can also produce surface waves propagating along a helical metasurface [21]. However, the volume effects in many 3D optical structures are complicated and difficult to modulate. Compared with volume effect, analyzing and understanding the surface effect of 3D curved structures from two-dimensional perspective by using transformation optics [22, 23] is a better approach. In order to confine light on the curved surface without considering the out-plane interference in experiments, just focusing on the ray dynamics on curved surface [24, 25] or adding curved surface boundary conditions [21, 26, 27] are needed. Obviously, better methods of observing curved surface effects are highly desired but remains unexplored. Moreover, some exotic optical phenomena based on curved structure often require complex permittivity and permeability, which makes it difficult for existing metamaterial technology or natural materials to achieve them [28–32]. However, under the influence of the large wavevectors, the strong surface modes can be excited by the curved polaritons without using external limits [33]. In addition, influenced by the ultrathin-slab approximation, the direction of wavevectors only depends on the ratio of permittivity in plane [11, 34–36], which greatly reduces the complexity of experiments. Therefore, polaritons based on layered materials are likely to become an important method for regulating the curved surface field in future [37, 38].

In this paper, we theoretically demonstrate the propagation properties based on curved anisotropic polaritons from ray dynamics and wave optics. We assume and analyze the elliptic and hyperbolic anisotropic Maxwell fish-eye metrics in which the symbols of in-plane coefficients are set to be same or opposite. Based on transformation optics [39–42], the radial elliptical and hyperbolic waves on the plane are projected onto the sphere surface and are excited as anisotropic polaritons. Additionally, we reveal the strong attraction of the poles on the hyperbolic anisotropic sphere surface to photons in terms of particle potential energy and equivalent optical refractive index profiles. The proposed curved anisotropic polaritons provide an important reference for developing curved surface field regulation with simple structure and multiple degrees of freedom, which can be generalized to more three-dimensional structures, such as cone and ring structures, and find new applications in photonics [43], for example, black hole [44], optical chaos [45], and meta-optical imaging [46].

2 Maxwell fisheye metric and curved polaritons

In mathematics, the Riemannian metric, g, in a 2D space can be written as $g = g_{ij}\,\mathrm{d}x^i\,\mathrm{d}x^j$ (with i and j ranging from 1 to 2) and $g_{12} = g_{21}$ in a certain coordinate system $(x^1,\ x^2)$. Hence, the line element is expressed by $\mathrm{d}s^2 = g_{11}\mathrm{d}x_1\mathrm{d}x_1 + 2g_{12}\mathrm{d}x_1\mathrm{d}x_2 + g_{22}\mathrm{d}x_2\mathrm{d}x_2$. Here we consider a concrete plane equipped with the 2D Euclidean metric $g_0 = \mathrm{d}\rho \otimes \mathrm{d}\rho + \rho^2\mathrm{d}\varphi \otimes \mathrm{d}\varphi$ in the polar coordinates, where ρ and φ are the radial coordinate and the angle coordinate, respectively. Such a flat plane can also be endowed with a non-Euclidean Riemannian metric, $g_1 = n(\rho,\ \theta)^2 g_0$. Hence g_0 and g_1 are conformally equivalent to each other. As we can see, $n(\rho,\ \theta)$ is the length scaling e^u, where u is a special choice with rotational symmetry. In order to solve the geodesics in the plane with the non-Euclidean metric, we consider the two-dimensional geodesic equation:

$$\frac{\mathrm{d}^2x^\lambda}{\mathrm{d}t^2} + \Gamma^\lambda_{uv}\frac{\mathrm{d}x^u}{\mathrm{d}t}\frac{\mathrm{d}x^v}{\mathrm{d}t} = 0, \tag{1}$$

where $\{\lambda,\ \mu,\ \nu\}$ are dummy indices (only with values 1 or 2), Γ^λ_{uv} are Christoffel symbol of the second kind in Riemannian physical space, and t is the length parameter of the geodesics. Christoffel symbol [47] can be obtained from the metric, namely,

$$\Gamma^\lambda_{uv} = g^{\lambda\omega}(\partial_v g_{u\omega} + \partial_u g_{v\omega} - \partial_\omega g_{uv})/2, \tag{2}$$

where $g^{\lambda\omega}$ is the component of the inverse of the metric $\boldsymbol{g}$.

Once we treat $n(\rho)$ as refractive index profile with rotational symmetry, $\mathrm{d}s^2$ represents the optical path. In the limit of geometric optics, the light rays follow the

Fermat principle, which states that light travels through the path in which it can reach the destination in the least time (compared with other nearby paths). Based on transformation optics, we can also obtain the equivalent relationship between the metric and the relative electromagnetic parameters [48]:

$$\varepsilon^{ij} = \mu^{ij} = \pm\sqrt{g}g^{ij}, \tag{3}$$

where the permittivity ε and the permeability μ are given in terms of the geometry.

Firstly, we consider an anisotropic two-dimensional radial metric:

$$\mathrm{d}s^2 = M\left(\frac{2}{\rho^2+1}\right)^2\mathrm{d}\rho^2 + N\left(\frac{2\rho}{\rho^2+1}\right)^2\mathrm{d}\varphi^2, \tag{4}$$

where M and N are anisotropic coefficients respectively. Here we define geometric parameter $\alpha = \sqrt{\frac{N}{M}}$. In previous studies [49], the geodesic in Eq. (4) is equal to the ray of the optical Maxwell fish-eye lenses when $M = N = 1$. To understand the anisotropic geometry, we compare the interval in Eq. (4) with the line element in Maxwell's fish-eye space: $\mathrm{d}s^2 = n^2\mathrm{d}l^2 = \left(\frac{2}{\rho'^2+1}\right)^2\mathrm{d}\rho'^2 + \left(\frac{2\rho'}{\rho'^2+1}\right)^2\mathrm{d}\varphi'^2$. It is easy to find that the interval in Eq. (4) can be obtained by the following transformation on the angular coordinate: $\rho' = \rho, \varphi' = \alpha\varphi$. Maxwell fish-eye lenses are optical absolute lenses, so all the geodesic rays are closed.

The above metric requires electromagnetic parameters that are both anisotropic and inhomogeneous, which is very difficult to achieve experimentally. Previous studies have shown that the stereographic projection of geodesic on spindle or sphere surface onto plane corresponds exactly to the rays in the generalized Maxwell fish-eye lens [43]. In this case, a homogeneous anisotropic curved surface is constructed, and the anisotropic Maxwell fish-eye line element is equivalent to an anisotropic curved line element by an inverse projection of light:

$$\begin{aligned}\mathrm{d}s^2 &= M\left(\frac{2}{\rho^2+1}\right)^2\mathrm{d}\rho^2 + N\left(\frac{2\rho}{\rho^2+1}\right)^2\mathrm{d}\varphi^2 \\ &= M\mathrm{d}\theta^2 + N\sin^2\theta\mathrm{d}\varphi^2 \\ &= \frac{M}{q}(q\mathrm{d}\theta^2) + N\sin^2\theta\mathrm{d}\varphi^2,\end{aligned} \tag{5}$$

where q=1 corresponds to the anisotropic spherical surfaces and $q > 1$ correspond to anisotropic spindle surfaces with different curvatures. Among them, their geodesic relationships are $h(\rho) = \arcsin\rho$ and $h(\rho) = \arcsin(\sqrt{q}\rho)$ respectively [see Fig. 1(a)]. Therefore, the spindle and the sphere have the same geodesic physics because their same line elements. For convenience, here we consider the light projection from sphere surface onto plane by using the north pole O as the projection point, as shown in Fig. 1(b). According to the projection operation, the initial point E′, central point S′ and point at infinity O′ on the plane correspond to the equatorial point E, south pole S and north pole O on the sphere surface, respectively.

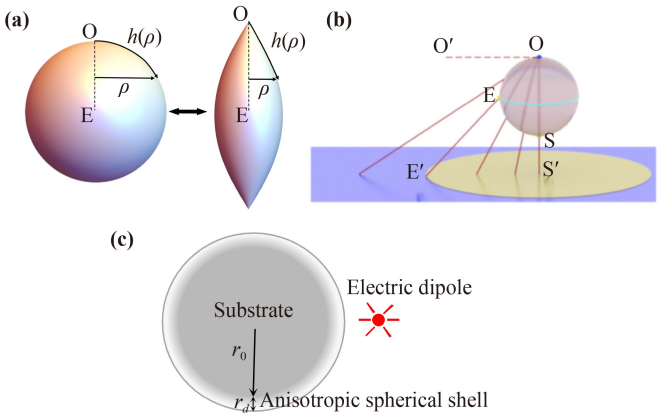

Fig. 1 **(a)** Spherical and spindle geodesic lenses. ρ is the radial coordinate, and $h(\rho)$ is the length measured along the meridian from O pole on the geodesic surface. **(b)** Schematic projection from sphere to Maxwell's fish-eye plane. **(c)** Schematic model of curved anisotropic polaritons.

In the above analysis, we concentrate on the geometrical aspect of in-plane anisotropy. Nevertheless, we cannot ignore the volume effect of the anisotropic sphere in the wave simulation. It is well known that the three-dimensional optical field modes are the superposition states of transverse electric (TE) and transverse magnetic (TM) modes. According to Eq. (3), the ideal three-dimensional wave realization of the above spherical metric requires both permittivity and permeability. Obviously, it is not practical to achieve them for both natural anisotropic materials and metamaterials. However, because of the approximation of large wavevectors and ultrathin-slab, curved anisotropic polaritons require only one of anisotropic permittivity or permeability tensors and can confine light on the curved surface without external absorbing conditions. In this case, polaritons become the indispensable carriers to excite designed curved surface patterns. Here, we excite curved polaritons in anisotropic spherical shell by an electric dipole, as shown in Fig. 1(c).

Additonally, any realistic systems should include losses or gains to fulfill the causality principle. Therefore, anisotropy ratio α can be complex valued if losses or gains are taken into consideration. However, the space-time geometry must be real. In the language of transformation optics, if the coordinate transformation is generalized to complex coordinates [50–52], the transformed material parameters become complex functions of the space coordinates. But this approach does not influence the effective geometry of the anisotropy. In addition, previous studies have also shown that small material losses will not affect the wavefront shape and propagation characteristics, only the propagation distance of in-plane

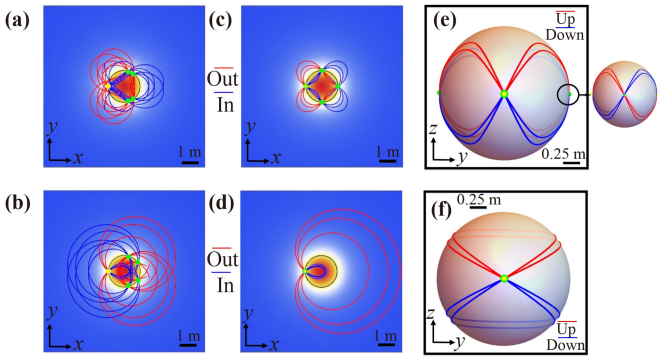

Fig. 2 Geodesics on the elliptical Maxwell's fish-eye plane for anisotropic coefficients. **(a)** $M = 1$, $N = 2$ ($\alpha = \sqrt{2}$). **(b)** $M = 2$, $N = 1$ ($\alpha = \sqrt{0.5}$). **(c)** M =1, $N = 4$ ($\alpha = 2$). **(d)** $M = 4$, $N = 1$ ($\alpha = 0.5$). Geodesics on the elliptical anisotropic sphere surface for anisotropic coefficients. **(e)** $M = 1$, $N = 4$ ($\alpha = 2$). **(f)** $M = 4$, N =1 ($\alpha = 0.5$). The yellow points are the sources and the green points are images. The red ray represents the light incident outside the circle (along the upward direction), and the blue ray represents the light incident inside the circle (along the downward direction). In subgraphs (a–d), the black circle bound is $|\rho| = 1$. The illustration of subgraph (e) is side view.

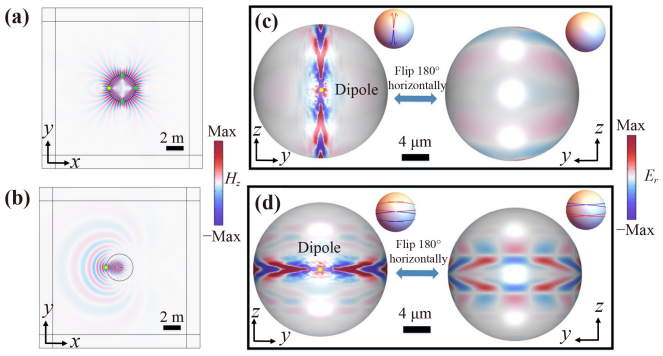

Fig. 3 The magnetic field H_z on the elliptical Maxwell's fish-eye plane for anisotropic permittivity. **(a)** $\varepsilon_\rho = 4[2/(\rho^2 + 1)]^2$, ε_φ =$[2/(\rho^2 + 1)]^2$. **(b)** $\varepsilon_\rho = [2/(\rho^2 + 1)]^2$, $\varepsilon_\varphi = 4\ [2/(\rho^2 + 1)]^2$. The electric field E_r on the elliptical anisotropic sphere surface for different anisotropic permittivity. **(c)** Front view and rear view for $\varepsilon_\theta = -38.2 - 7.07$i, $\varepsilon_\varphi = -0.24 - 0.11$i. **(d)** Front view and rear view for $\varepsilon_\theta = -0.24 - 0.11$i, $\varepsilon_\varphi =$ –38.2 – 7.07i. The yellow points are the sources and the green points are images. In subgraphs (a, b), the incident wavelength λ is set as 0.5 m (m could be arbitrary unit), the black circle bound is $|\rho| = 1$ and the outermost layer structures are perfectly matched layers. In subgraphs (c, d), the radius of the inner sphere, the thickness of elliptical anisotropic spherical shell, and the incident wavelength are set as $r_0 =$ 10 μm, $r_d = 300$ nm, $\lambda = 11.92$ μm. The illustrations are the geodesics whose metric corresponding to the real part of the permittivity.

anisotropic polaritons [11, 36]. Considering the loss of real systems, next we will discuss curved anisotropic polaritons in naturally anisotropic materials MoO_3.

3 Curved elliptical polaritons

Here, we consider the case $\mathrm{sgn}(M) = \mathrm{sgn}(N)$ and $M \neq N$. Frist, we assume the elliptical Maxwell's fish-eye plane and sphere corresponding to the metrics in Eqs. (4) and (5). For convenience, we set the cicle $|\rho|$=1 m (equator $\theta = \pi/2$) as the initial position of ray and calculate the geodesics [see the Electronic Supplementary Materials (ESM)] for different geometric parameters, as shown in Fig. 2.

According to the geodesic projection, the rays incident outside (inside) the circle correspond to the light along the upward (downward) direction. Thus, the image points on the circle correspond to the image points on the spherical equator. When α is rational number ($\alpha = 2$, 0.5), the rays will propagate along the periodic orbits with self-focusing phenomena. Therefore, only a finite number of images on the circle, and the number of images is dependent on α; Otherwise, caustics will occur ($\alpha = \sqrt{2}, \sqrt{0.5}$). In the ESM, we find that α corresponds exactly to the scaling parameter in generalized Maxwell' s fish-eye lens. The rationality of the scaling parameters has been shown to affect the self-focusing of the lens in previous work [53], and our findings demonstrate that the rationality of the anisotropy ratio can have a similar effect.

Then we design and simulate the elliptical inhomogeneous wave to verify the in-plane geodesics in Figs. 2(c) and (d) by the finite-element methods. In two-dimensional transverse magnetic (TM) modes, we only need to consider (E_ρ, E_φ, H_z). Therefore, based on Eq. (3), we set $(\varepsilon_\rho, \varepsilon_\varphi, \mu_z) = (N(\frac{2}{\rho^2+1})^2, M(\frac{2}{\rho^2+1})^2, 1)$. Similar to ray tracing, we place a point source at (–1, 0) m as the excitation source of TM waves. When $\alpha = 2$, under the influence of anisotropic permittivity, the radial elliptic waves show square symmetry, indicating that there are three other image points on the circle [see Fig. 3(a)]. In addition, we can see clear propagation fringes near the circle, but they do not interfere with each other to form image points when $\alpha = 0.5$.

The anisotropic polaritons are selected to investigate the in-plane elliptic anisotropic effect on the curved surface. It is worth noting that, unlike two-dimensional elliptic waves, the permittivity of the elliptic anisotropic polaritons we discuss next is negative. Here we set the incident wavelength $\lambda = 11.92$ μm, the substrate material and the background material are set as air. Considering the thickness of the van der Waals films and the excitation of the in-plane polaritons, the radius of the inner sphere $r_0 = 10$ μm, and the thickness of anisotropic spherical shell $r_d = 300$ nm. We place an electric dipole above the equator and observe out-of-plane electric field E_r on the sphere surface. Depending on the direction of winding, the relative electromagnetic permittivities of MoO_3 [11]

spherical shell $(\varepsilon_r, \varepsilon_\theta, \varepsilon_\varphi)$ are set as $(5.6-0.02\mathrm{i}, -38.2-7.07\mathrm{i}, -0.24-0.11\mathrm{i})$ in Fig. 3(c), and $(5.6-0.02\mathrm{i}, -0.24-0.11\mathrm{i}, -38.2-7.07\mathrm{i})$ in Fig. 3(d). Previous studies have shown that bending two-dimensional materials produces modes with different field confinement and the lowest mode is very localized at the curved waveguide's vertex [54]. Therefore, affected by modes and material losses, our in-plane polaritons are also localized at partial sphere. In order to explain the phenomenon of elliptic polaritons on the sphere, we show the corresponding ray behavior over a short period of time in the illustrations of Figs. 3(c) and (d). By comparing Figs. 3(c) and (d) with their illustrations, we can still see the clear influence of anisotropic parameters on polariton propagation. When $|\varepsilon_\theta| < |\varepsilon_\varphi|$, the horizontal elliptic polaritons will form parallel propagation fringes near the equator, which can be used for information transmission and construction of new light fields on curved surfaces. Due to curvature and extreme anisotropy, the vertical elliptic polaritons do not propagate to the other side of the sphere, resulting in a local channelization effect.

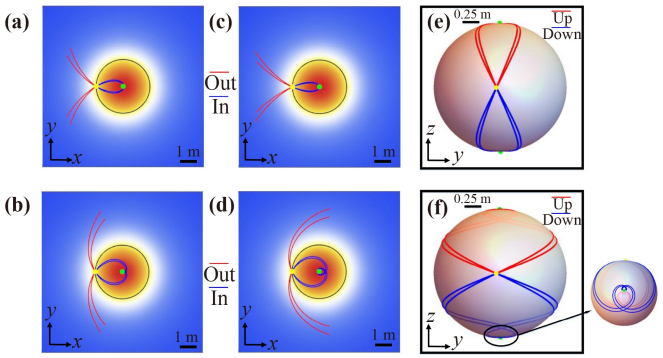

Fig. 4 Geodesics on the hyperbolic Maxwell's fish-eye plane for anisotropic coefficients. **(a)** $M = 1$, $N = -2$ ($\alpha = \mathrm{i}\sqrt{2}$). **(b)** $M = -2$, $N = 1$($\alpha = \mathrm{i}\sqrt{0.5}$). **(c)** $M = 1$, $N = -4$ ($\alpha = 2\mathrm{i}$). **(d)** $M = -4$, $N = 1$ ($\alpha = 0.5\mathrm{i}$). Geodesics on the hyperbolic anisotropic sphere surface for anisotropic coefficients. **(e)** $M = 1$, $N = -4$ ($\alpha = 2\mathrm{i}$). **(f)** $M = -4$, $N = 1$ ($\alpha = 0.5\mathrm{i}$). The yellow points are the sources and the green points are images. The red ray represents the light incident outside the circle (along the upward direction), and the blue ray represents the light incident inside the circle (along the downward direction). In subgraphs (a– d), the black circle bound is $|\rho| = 1$. The illustration of subgraph (f) is upward view.

4 Curved hyperbolic polaritons

Similarly, we change the symbols of M or N and remain the value of $|\alpha|$. For this case, there is no intuitive geometric picture, such as ordinary disclination described above, because the spatial metric is no longer definitely positive when α^2 is negative. Actually, the coordinate with a negative metric component behaves as a time-like coordinate that turns the effective geometry of the anisotropic medium from Riemannian space to a pseudo-Riemannian space. As shown in Fig. 4, rays incident inside the circle (along the downward direction) will focus on the center (south pole) while rays incident outside the circle (along the upward direction) move away from the center of the circle gradually and arrive at the infinity (north pole). Unlike the case of elliptic anisotropy in Fig. 2, the self-focusing properties and caustics of light do not occur regardless of whether $|\alpha|$ is rational or not. When $|\alpha^2|$ is larger than 1, the rays are very similar to the intersection lines left by an elliptic cylinder embedded in a sphere, i.e., Viviani's curves. When $|\alpha^2|$ is less than 1, we can see the spirals clearly at the poles of the sphere or the center of the circle [see Figs. 4(b), (d) and (f)]). In the ESM, we discuss the equivalent potential nergy and refractive index profiles of hyperbolic sphere surface. The results reveal that, the equivalent potential energy and refractive index at $\theta = 0$ (south pole) and $\theta = \pi$ (north pole) are infinite (black hole medium), in other words, poles are extremely attractive to photons. Therefore, it is obvious that the hyperbolic electromagnetic parameters form an effective curved black hole.

In order to verify the above geodesics in wave optics, we design and simulate the hyperbolic inhomogeneous wave by the finite-element methods. Similar to elliptic wave, we place a point source at the cicle $|\rho| = 1$ m (equator $\theta = \pi/2$) as the excitation source of TM waves. As shown in Figs. 5(a) and (b), hyperbolic waves converging at the center or diverging to infinity, which are consistent with the ray results in Fig. 4. In the propagation of hyperbolic waves [11], the value of $|\alpha^2|$ influence the open angle and direction of hyperbolic waves. When $|\alpha^2|$ is larger than 1, waves incident inside the circle are all caught in the center of the circle [see Fig. 5(a)]. Meanwhile, the hyperbolic waves outside the circle are confined within an open angle and have long lifetimes, which preserve the properties of the traditional hyperbolic waves. When $|\alpha|$ is less than 1, we can also clearly see the spiral light field inside the circle in Fig. 5(b). Interestingly, our ray analysis and wave simulation also show the helical light field and optical singularity based on the radial hyperbolic plane [18, 55].

Based the same structure with Fig. 1(c), here we excite the curved polaritons at the incident wavelength $\lambda = 11.05$ μm and the simulation results based on finite-element methods are shown in Figs. 5(c) and (d). Depending on the direction of winding, the relative electromagnetic parameters of MoO_3 [11] spherical shell $(\varepsilon_r, \varepsilon_\theta, \varepsilon_\varphi)$ are set as $(7.96-0.07\mathrm{i}, -4.04-0.34\mathrm{i}, 1.02-0.07\mathrm{i})$ in Fig. 5(c), and $(7.96-0.07\mathrm{i}, 1.02-0.07\mathrm{i}, -4.04-0.34\mathrm{i})$ in Fig. 5(d). As shown in Fig. 5, the curved hyperbolic polaritons can be localized perfectly on the sphere and retain the properties of geodesic manifold in Fig. 4 without almost being affected by material losses. Unlike the bulk

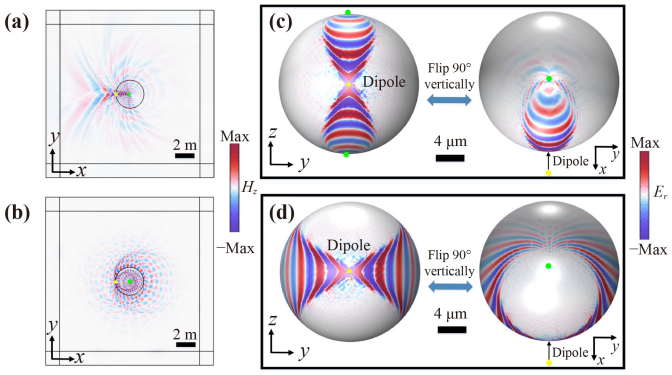

Fig. 5 The magnetic field H_z on the hyperbolic Maxwell's fish-eye plane for anisotropic permittivity. **(a)** $\varepsilon_\rho = -4[2/(\rho^2+1)]^2$, $\varepsilon_\varphi = [2/(\rho^2+1)]^2$. **(b)** $\varepsilon_\rho = [2/(\rho^2+1)]^2$, $\varepsilon_\varphi = -4\,[2/(\rho^2+1)]^2$. The electric field E_r on the hyperbolic anisotropic sphere surface for different anisotropic permittivity. **(c)** Front view and top view for $\varepsilon_\theta = -4.04 - 0.34\mathrm{i}$, $\varepsilon_\varphi = 1.02 - 0.07\mathrm{i}$. **(d)** Front view and top view for $\varepsilon_\theta = 1.02 - 0.07\mathrm{i}$, $\varepsilon_\varphi = -4.04 - 0.34\mathrm{i}$. The yellow points are the sources and the green points are images. In subgraphs (a, b), the incident wavelength λ is set as 0.5m (m could be arbitrary unit), the black circle bound is $|\rho| = 1$ and the outermost layer structures are perfectly matched layers. In subgraphs (c, d), the radius of the inner sphere, the thickness of hyperbolic spherical shell, and the incident wavelength are set as $r_0 = 10$ μm, $r_\mathrm{d} = 300$ nm, $\lambda = 11.05$ μm.

effect of hyperbolic materials [56], the hyperbolic wavefront does not propagate to the other side of the sphere to form periodic orbits, but focuses on the poles of the sphere surface. It is worth mentioning that, affected by the high refractive index of the center, the light field near the pole will be bounced off and produce interference fringes [see Fig. 5(e)]. In the ESM, we show the response to the dipoles at other positions and the metastructure realization of hyperbolic curved polaritons.

5 Discussion

In this paper, the above discussion does not consider the effect of substrate materials because the propagation of curved polaritons mainly depends on the in-plane permittivity tensor of the anisotropic spherical shell. Inevitably, excessive refractive index difference between environment and substrate material will disturb the stability of the waveguide mode and cause a little clutter. Nevertheless, common substrates (such as SiO_2/Si) do not influence the propagation of the anisotropic polaritons on the curved surface. In addition, the forms of the permittivity tensor in different coordinate systems are different. Therefore, we mentioned the conversion of the permittivity tensor between the different curved coordinates and the Cartesian coordinates in the ESM.

Existing 2D material systems can only achieve anisotropic in-plane elliptic dispersion (ε_x, $\varepsilon_y < 0$ & $\varepsilon_x \neq \varepsilon_y$) in narrow frequency bands, and it is usually extremely anisotropic ($\varepsilon_x \gg \varepsilon_y$). In contrast, many two-dimensional materials and metamaterials have recently been able to produce stable hyperbolic dispersion. Comparing with curved hyperbolic polaritons, curved elliptic polaritons have longer propagation distances and become more susceptible to material loss and mode loss. Therefore, the curved hyperbolic polaritons are of higher application value and experimental realizability. Here we consider natural hyperbolic films MoO_3 as the shell material because it supports both in-plane elliptical and hyperbolic anisotropic polaritons in the infrared band. Recent research [57] suggests that the two-dimension boron nitride sheet can be grown by chemical vapour deposition and inherit the hyperbolic phonon–polariton dispersion of hexagonal boron nitride. In addition, transition-metal nitride superlattices on F-mica can be substantially bent via reactive magnetron sputtering and support hyperbolic response in the visible to near-infrared ranges [58], which implies the feasibility of wrapping two-dimensional hyperbolic van der Waals films or growing them on the curved substrates. Therefore, one can achieve a thin layer α-MoO_3 surrounding the sphere by wrapping the flakes/nanoribbons with careful control of the rolling angle. Besides, there are other possible approaches. For example, high-quality α-MoO_3 with large area can be directly grown on the SiO_2 substrate by a CVD method [59]. With the help of Scattering-type scanning near-field optical microscopy (s-SNOM) set-up and metallic atomic force microscopy-based infrared spectroscopy (AFM-IR) technique, one can observe the propagation and focusing behavior of anisotropic polariton by the Nano IR spectra and near-field two-dimensional imagings [57].

In summary, based on the anisotropic Maxwell fish-eye metric and projection, we introduce the anisotropic polaritons on curved surface and demonstrate their unique optical properties through ray tracing and wave simulations based natural anisotropic materials. Our paper provides valuable references for the applications of curved anisotropic polaritons on sphere/spindle surface and suggests that more curved surface, such as rings and cones, could serve as research platforms of anisotropic polaritons in the future.

Declarations The authors declare that they have no competing interests and there are no conflicts.

Author contributions All authors have accepted responsibility for the entire content of this manuscript and approved its submission.

Data availability Data underlying the results presented in this paper are not publicly available at this time but may be obtained from the authors upon reasonable request.

Electronic supplementary materials The online version contains supplementary material available at https://doi.org/10.1007/s11467-023-1360-9 and https://journal.hep.com.cn/fop/EN/10.1007/s11467-023-1360-9.

Acknowledgements We wish to thank Shan Zhu and Yali Zeng for helpful discussion. This research was funded by the National Natural Science Foundation of China (No. 92050102), the National Key Research and Development Program of China (No. 2020YFA0710100), the Fundamental Research Funds for the Central Universities (No. 2072023102), and the Jiangxi Provincial Natural Science Foundation (No. 20224ACB201005).

References

1. D. N. Basov, M. M. Fogler, and F. J. García de Abajo, Polaritons in van der Waals materials, *Science* 354(6309), aag1992 (2016)
2. T. Low, A. Chaves, J. D. Caldwell, A. Kumar, N. X. Fang, P. Avouris, T. F. Heinz, F. Guinea, L. Martin-Moreno, and F. Koppens, Polaritons in layered two-dimensional materials, *Nat. Mater.* 16(2), 182 (2017)
3. H. Raether, in: Surface Plasmons on Smooth and Rough Surfaces and on Gratings, Springer Tracts in Modern Physics, Vol. 111, Springer, 1988, pp 4–39
4. S. A. Maier, Plasmonics: Fundamentals and Applications, Springer, 2007, pp 21–37
5. Z. Dai, G. Hu, Q. Ou, L. Zhang, F. Xia, F. J. Garcia-Vidal, C. W. Qiu, and Q. Bao, Artificial metaphotonics born naturally in two dimensions, *Chem. Rev.* 120(13), 6197 (2020)
6. Z. Jin, D. Janoschka, J. Deng, L. Ge, P. Dreher, B. Frank, G. Hu, J. Ni, Y. Yang, J. Li, C. Yu, D. Lei, G. Li, S. Xiao, S. Mei, H. Giessen, F. M. zu Heringdorf, and C. W. Qiu, Phyllotaxis-inspired nanosieves with multiplexed orbital angular momentum, *eLight* 1, 5 (2021)
7. A. Woessner, M. B. Lundeberg, Y. Gao, A. Principi, P. Alonso-González, M. Carrega, K. Watanabe, T. Taniguchi, G. Vignale, M. Polini, J. Hone, R. Hillenbrand, and F. H. L. Koppens, Highly confined low-loss plasmons in graphene-boron nitride heterostructures, *Nat. Mater.* 14(4), 421 (2015)
8. T. Low, R. Roldán, H. Wang, F. Xia, P. Avouris, L. M. Moreno, and F. Guinea, Plasmons and screening in monolayer and multilayer black phosphorus, *Phys. Rev. Lett.* 113(10), 106802 (2014)
9. E. Yoxall, M. Schnell, A. Y. Nikitin, O. Txoperena, A. Woessner, M. B. Lundeberg, F. Casanova, L. E. Hueso, F. H. L. Koppens, and R. Hillenbrand, Direct observation of ultraslow hyperbolic polariton propagation with negative phase velocity, *Nat. Photonics* 9(10), 674 (2015)
10. Z. Zheng, J. Chen, Y. Wang, X. Wang, X. Chen, P. Liu, J. Xu, W. Xie, H. Chen, S. Deng, and N. Xu, Highly confined and tunable hyperbolic phonon polaritons in van der Waals semiconducting transition metal oxides, *Adv. Mater.* 30(13), 1705318 (2018)
11. W. Ma, P. Alonso-González, S. Li, A. Y. Nikitin, J. Yuan, J. Martín-Sánchez, J. Taboada-Gutiérrez, I. Amenabar, P. Li, S. Vélez, C. Tollan, Z. Dai, Y. Zhang, S. Sriram, K. Kalantar-Zadeh, S. T. Lee, R. Hillenbrand, and Q. Bao, In-plane anisotropic and ultra-low-loss polaritons in a natural van der Waals crystal, *Nature* 562(7728), 557 (2018)
12. Z. Fei, M. E. Scott, D. J. Gosztola, J. J. Foley, J. Yan, D. G. Mandrus, H. Wen, P. Zhou, D. W. Zhang, Y. Sun, J. R. Guest, S. K. Gray, W. Bao, G. P. Wiederrecht, and X. Xu, Nano-optical imaging of WSe_2 waveguide modes revealing light–exciton interactions, *Phys. Rev. B* 94(8), 081402 (2016)
13. G. Lu, Z. Pan, C. R. Gubbin, R. A. Kowalski, S. De Liberato, D. Li, and J. D. Caldwell, Launching and manipulation of higher-order in-plane hyperbolic phonon polaritons in low-dimensional heterostructures, *Adv. Mater.* 35(22), 2300301 (2023)
14. L. Ma, A. Ge, L. Sun, F. Liu, and W. Lu, Focusing of hyperbolic phonon polaritons by bent metal nanowires and their polarization dependence, *ACS Photonics* 10(6), 1841 (2023)
15. C. Hu, T. Sun, Y. Zeng, W. Ma, Z. Dai, X. Yang, X. Zhang, and P. Li, Source-configured symmetry-broken hyperbolic polaritons, *eLight* 3, 14 (2023)
16. M. Durach, R. Williamson, J. Adams, T. Holtz, P. Bhatt, R. Moreno, and F. Smith, On Fresnel–Airy equations, Fabry–Perot resonances and surface electromagnetic waves in arbitrary bianisotropic metamaterials, *Electromagn. Waves* 173, 53 (2022)
17. L. Song, L. Shen, and H. Wang, Squeezing of hyperbolic polaritonic rays in cylindrical lamellar structures, *Electromagn. Waves* 174, 23 (2022)
18. F. dos S. Azevedo, J. D. M. de Lima, A. de Pádua Santos, and F. Moraes, Optical wormhole from hollow disclinations, *Phys. Rev. A* 103(2), 023516 (2021)
19. Y. Wang, Y. Ren, X. Luo, B. Li, Z. Chen, Z. Liu, F. Liu, Y. Cai, Y. Zhang, J. Liu, and F. Li, Manipulating cavity photon dynamics by topologically curved space, *Light Sci. Appl.* 11(1), 308 (2022)
20. F. D. S. Azevedo, D. Figueiredo, F. Moraes, B. Berche, and S. Fumeron, Optical concentrator from a hyperbolic liquid-crystal metamaterial, *EPL* 124(3), 34006 (2018)
21. Y. Mazor and A. Alù, Angular-momentum selectivity and asymmetry in highly confined wave propagation along sheath-helical metasurface tubes, *Phys. Rev. B* 99(15), 155425 (2019)
22. U. Leonhardt, Optical conformal mapping, *Science* 312(5781), 1777 (2006)
23. J. B. Pendry, D. Schurig, and D. R. Smith, Controlling electromagnetic fields, *Science* 312(5781), 1780 (2006)
24. L. Xu, X. Wang, T. Tyc, C. Sheng, S. Zhu, H. Liu, and H. Chen, Light rays and waves on geodesic lenses, *Photon. Res.* 7(11), 1266 (2019)
25. L. Xu, R. He, K. Yao, J. M. Chen, C. Sheng, Y. Chen, G. Cai, S. Zhu, H. Liu, and H. Chen, Conformal singularities and topological defects from inverse transformation optics, *Phys. Rev. Appl.* 11(3), 034072 (2019)
26. Y. Yin, Q. Duan, J. Li, C. Qiu, and H. Chen, Evolution of optical vortices in gradient media and curved spaces, *Opt. Lett.* 48(2), 315 (2023)
27. Z. Sun, Á. Gutiérrez-Rubio, D. N. Basov, and M. M. Fogler, Hamiltonian optics of hyperbolic polaritons in

nanogranules, *Nano Lett.* 15(7), 4455 (2015)
28. H. Chen, B. I. Wu, B. Zhang, and J. A. Kong, Electromagnetic wave interactions with a metamaterial cloak, *Phys. Rev. Lett.* 99(6), 063903 (2007)
29. B. Zhang, B. I. Wu, H. Chen, and J. A. Kong, Rainbow and blueshift effect of a dispersive spherical invisibility cloak impinged on by a nonmonochromatic plane wave, *Phys. Rev. Lett.* 101(6), 063902 (2008)
30. B. Zhang, H. Chen, B. I. Wu, and J. A. Kong, Extraordinary surface voltage effect in the invisibility cloak with an active device inside, *Phys. Rev. Lett.* 100(6), 063904 (2008)
31. M. Zhou, L. Xu, L. Zhang, J. Wu, Y. Li, and H. Chen, Perfect invisibility concentrator with simplified material parameters, *Front. Phys.* 13(4), 134101 (2018)
32. P. F. Zhao, L. Xu, G. X. Cai, N. Liu, and H. Y. Chen, A feasible approach to field concentrators of arbitrary shapes, *Front. Phys.* 13(4), 134205 (2018)
33. G. Álvarez-Pérez, K. V. Voronin, V. S. Volkov, P. Alonso-González, and A. Y. Nikitin, Analytical approximations for the dispersion of electromagnetic modes in slabs of biaxial crystals, *Phys. Rev. B* 100(23), 235408 (2019)
34. G. Hu, A. Krasnok, Y. Mazor, C. W. Qiu, and A. Alù, Moiré hyperbolic metasurfaces, *Nano Lett.* 20(5), 3217 (2020)
35. G. Hu, J. Shen, C. W. Qiu, A. Alù, and S. Dai, Phonon polaritons and hyperbolic response in van der Waals materials, *Adv. Opt. Mater.* 8(5), 1901393 (2020)
36. G. Hu, Q. Ou, G. Si, Y. Wu, J. Wu, Z. Dai, A. Krasnok, Y. Mazor, Q. Zhang, Q. Bao, C. W. Qiu, and A. Alù, Topological polaritons and photonic magic angles in twisted α-MoO_3 bilayers, *Nature* 582(7811), 209 (2020)
37. T. P. Rasmussen, P. A. D. Gonçalves, S. Xiao, S. Hofferberth, N. A. Mortensen, and J. D. Cox, Polaritons in two-dimensional parabolic waveguides, *ACS Photonics* 8(6), 1840 (2021)
38. H. Hu, R. Yu, H. Teng, D. Hu, N. Chen, Y. Qu, X. Yang, X. Chen, A. S. McLeod, P. Alonso-González, X. Guo, C. Li, Z. Yao, Z. Li, J. Chen, Z. Sun, M. Liu, F. J. García de Abajo, and Q. Dai, Active control of micrometer plasmon propagationin suspended graphene, *Nat. Commun.* 13(1), 1465 (2022)
39. U. Leonhardt, Optical conformal mapping, *Science* 312(5781), 1777 (2006)
40. J. B. Pendry, D. Schurig, and D. R. Smith, Controlling electromagnetic fields, *Science* 312(5781), 1780 (2006)
41. Z. Xiong, L. Xu, Y. Xu, and H. Chen, Broadband illusion optical devices based on conformal mappings, *Front. Phys.* 12(5), 124202 (2017)
42. L. Xu, Q. Wu, Y. Zhou, and H. Chen, Transformation devices with optical nihility media and reduced realizations, *Front. Phys.* 14(4), 42501 (2019)
43. Z. Chen and M. Segev, Highlighting photonics: Looking into the next decade, *eLight* 1, 2 (2021)
44. Q. Ba, Y. Zhou, J. Li, W. Xiao, L. Ye, Y. Liu, J. Chen, and H. Chen, Conformal optical black hole for cavity, *eLight* 2, 19 (2022)
45. T. Hou and H. Chen, Anisotropic kepler problem in a non-rotationally-symmetric eaton lens, *Phys. Rev. A* 105(4), 043501 (2022)
46. J. E. Fröch, L. Huang, Q. A. Tanguy, S. Colburn, A. Zhan, A. Ravagli, E. J. Seibel, K. F. Böhringer, and A. Majumdar, Real time full-color imaging in a meta-optical fiber endoscope, *eLight* 3, 13 (2023)
47. M. P. Hobson, G. P. Efstathiou, and A. N. Lasenby, General Relativity: An Introduction for Physicists, Cambridge University Press, Cambridge, UK, 2006
48. L. Ulf and T. Philbin, Geometry and Light: The Science of Invisibility, Courier Corporation, 2010
49. L. Xu, W. Xiao, L. Zhang, J. Li, J. Zhou, and H. Chen, Observation of light rays on absolute geodesic lenses, *Opt. Express* 28(14), 20215 (2020)
50. G. Castaldi, S. Savoia, V. Galdi, A. Alu, and N. Engheta, *PT* metamaterials via complex-coordinate transformation optics, *Phys. Rev. Lett.* 110(17), 173901 (2013)
51. B. I. Papa and S. A. Cummer, Complex coordinates in transformation optics, *Phys. Rev. A* 84(6), 063837 (2011)
52. S. Savoia, G. Castaldi, and V. Galdi, Complex-coordinate non-Hermitian transformation optics, *J. Opt.* 18(4), 044027 (2016)
53. H. Chen, Imaging along conformal curves, *Phys. Rev. A* 98(4), 043843 (2018)
54. D. Smirnova, S. H. Mousavi, Z. Wang, Y. S. Kivshar, and A. B. Khanikaev, Trapping and guiding surface plasmons in curved graphene landscapes, *ACS Photonics* 3(5), 875 (2016)
55. Z. Jacob, L. V. Alekseyev, and E. Narimanov, Semiclassical theory of the hyperlens, *J. Opt. Soc. Am. A* 24(10), A52 (2007)
56. Z. Sun, Á. Gutiérrez-Rubio, D. N. Basov, and M. M. Fogler, hamiltonian optics of hyperbolic polaritons in nanogranules, *Nano Lett.* 15(7), 4455 (2015)
57. X. Guo, N. Li, X. Yang, R. Qi, C. Wu, R. Shi, Y. Li, Y. Huang, F. J. García de Abajo, E. G. Wang, P. Gao, and Q. Dai, Hyperbolic whispering-gallery phonon polaritons in boron nitride nanotubes, *Nat. Nanotechnol.* 18(5), 529 (2023)
58. R. Zhang, T. Lin, S. Peng, J. Bi, S. Zhang, G. Su, J. Sun, J. Gao, H. Cao, Q. Zhang, L. Gu, and Y. Cao, Flexible but refractory single-crystalline hyperbolic metamaterials, *Nano Lett.* 23(9), 3879 (2023)
59. Y. Wang, X. Du, J. Wang, M. Su, X. Wan, H. Meng, W. Xie, J. Xu, and P. Liu, Growth of large-scale, large-size, few-layered α-MoO_3 on SiO_2 and its photoresponse mechanism, *ACS Appl. Mater. Interfaces* 9(6), 5543 (2017)